PNAS
www.pnas.org

Supplementary Information for

An outer pore gate modulates the pharmacology of the TMEM16A channel

Ria L. Dinsdale, Tanadet Pipatpolkai, Emilio Agostinelli, Angela J. Russell, Phillip J. Stansfeld and Paolo Tammaro

Dr Paolo Tammaro or Dr Phillip Stansfeld
Email: paolo.tammaro@pharm.ox.ac.uk or phillip.stansfeld@warwick.ac.uk

This PDF file includes:

Other supplementary materials for this manuscript include the following:

Supplementary Information Text

Additions to the methods

Cell Culture, heterologous expression, and single point mutagenesis

This study involved mouse TMEM16A (isoform *a*) (1) subcloned into the pcDNA3.1 vector. Single point mutagenesis was done using the Quikchange® Lightning Site-directed Mutagenesis kit (Agilent Technologies, UK). HEK-293T cells were cultured as previously described (2) and transfected with 0.6 μg of plasmid DNA using Fugene HD (Promega, UK). The mutant TMEM16A-S513A had reduced expression, thus we used 1.2 μg of the corresponding plasmid for transfection. In some experiments, plasmid DNA was omitted (mock transfected) and these cells used as control. Cells were used ~1-2 days after transfection. Transfected cells were identified using the anti-CD8 antibody-coated beads method (2, 3).

Electrophysiology

TMEM16A currents were measured with the whole-cell or inside-out patch configuration of the patch-clamp technique using an Axon 200B amplifier (Molecular Devices, USA) controlled with GE-pulse software (http://users.ge.ibf.cnr.it/pusch/programs-mik.htm) with an external analogue-to-digital and digital-to-analogue converter (USB-6221, National Instruments, UK). Pipettes were pulled from borosilicate glass capillary tubes (Harvard Apparatus, UK) using a Narishige PC-10 pipette puller (Narishige, Japan). Pipette tip diameter yielded a resistance of 2-4 MΩ in the working solutions. The bath was grounded through a 3 M KCl agar bridge connected to an Ag–AgCl reference electrode. In whole-cell recordings, the series resistance was usually compensated to achieve a maximal effective resistance lower than 5-10 MΩ. Experiments were conducted at 20-22 °C. The cell capacitance was assessed by measuring the area under the capacitive transient elicited by a 10 mV voltage step or using the cell capacitance compensation circuit of the amplifier. In some experiments, whole-cell current recordings were normalised to cell capacitance to obtain current density (in pA/pF). Currents were filtered at 2 kHz or 5 kHz and sampled at 10 kHz. To allow for equilibration of the pipette solution with the cell interior, whole-cell recordings started >3 min after establishing the whole-cell configuration (4). The exchange of solutions was achieved by using a local perfusion system consisting of eight tubes of 1.2 mm diameter into which the tip of the patch pipette was inserted. In some experiments, ultra-rapid (<50 ms) changes in A9C concentration ([A9C]) ('concentration jumps') were achieved using a computer-controlled perfusion system (Warner Instruments, Hamden, CT, USA).

Composition of solutions

The extracellular solution contained (mM): 150 NaCl, 1 $CaCl_2$, 1 $MgCl_2$, 10 glucose, 10 D-mannitol and 10 HEPES; pH was adjusted to 7.4 with NaOH. The intracellular solution contained (mM): 130 CsCl, 10 EGTA, 1 $MgCl_2$, 10 HEPES and 4.5, 6.0, 7.5, or 8.0 mM $CaCl_2$ to obtain approximately 0.06, 0.10, 0.21, 0.27 μM free $[Ca^{2+}]$, pH was adjusted to 7.3 with NaOH. For intracellular solutions with higher $[Ca^{2+}]_i$, EGTA was replaced with equimolar HEDTA and 2.1, 3.1, 4.8, 7.8, 9, or 9.4 mM $CaCl_2$ were used to obtain approximately 0.60, 1.04, 2.30, 12.50, 78.0 and 195.1 μM free $[Ca^{2+}]$, respectively (calculated with Patcher's Power tool, Dr Francisco Mendez and Frank Wurriehausen,

Max-Planck-Institut für biophysikalische Chemie, Göttingen, Germany). Nominally Ca^{2+}-free intracellular solution was obtained by omitting $CaCl_2$ in the EGTA-containing intracellular solution. The intracellular solution in which Ca^{2+} was replaced with Gd^{3+} contained (mM): 100 CsCl, 1 $MgCl_2$, 1 EGTA, 10 HEPES and 5 $GdCl_3$; pH was adjusted to 7.3 with NaOH. D-mannitol was used to maintain osmolarity of all intracellular solution unchanged.

For determination of saturation and binding of Cl^- into the pore of the TMEM16A channel, CsCl in the intracellular solution was replaced with caesium methanesulfonate (Cs-MES) and the concentration of NaCl in the extracellular solution was adjusted to 6, 10, 30, 70, 160 and 360 (mM) while the concentration of D-mannitol was proportionally altered to maintain osmolarity of extracellular solution unchanged. A9C (Sigma, UK) was dissolved in DMSO (stock concentration, 100 mM) resulting in a concentration of <1% DMSO in the working solutions. The pH of the solutions containing working concentrations of A9C was adjusted to 7.4 with NaOH.

The $[Ca^{2+}]_i$ used for experiments in figures 2, 3, S1 and S2 was selected in order to obtain a comparable activation above the baseline (i.e. current measured in 0 Ca^{2+}) for TMEM16A, TMEM16A-Q645A and TMEM16A-I637A whole-cell currents. For TMEM16A, a $[Ca^{2+}]_i$ of 0.3 μM produced about 5 % of activation (Fig. 1D). To achieve similar level of activation above baseline for TMEM16A-Q645A and -I637A a $[Ca^{2+}]_i$ within the 0.05-0.1 μM range is required (Fig. 1D). In Fig. S10 we show that the effects of A9C measured in either 0.05 or 0.1 μM $[Ca^{2+}]_i$ were not statistically different. Thus, we used 0.1 μM $[Ca^{2+}]_i$ for any further experiments, because with this $[Ca^{2+}]_i$ the amplitude (in pA/pF) of the whole-cell currents for the mutant channels was similar to that of the whole-cell currents for the wild-type channel obtained in 0.3 μM $[Ca^{2+}]_i$ (Fig. S1).

Main stimulation protocols

Current versus V_m relationships:

Current *versus* V_m relationships were constructed by measuring currents in response to 1 s V_m steps from −100 to +100 mV in 20 mV increments elicited every 2 s from a holding V_m of 0 mV ('IV protocol'). In some experiments, 1 s V_m steps from -100 to +140 mV in 40 mV increments (test pulses) were elicited after a 1.5 s V_m step to +70 mV (pre-pulse) every 2 s from a holding V_m of 0 mV ('IV tail protocol'). As detailed in the results, in the presence of extracellular A9C, the test-pulse currents reached a peak within the first ~50 ms of the test pulse. These peak currents were normalised for the current of the pre-pulse and plotted against the V_m of the test pulse. For determination of the current reversal potential (E_{rev}), instantaneous currents were estimated from extrapolation of single exponential fits of the test-pulse currents to the beginning of each test pulse. These instantaneous current values were plotted *versus* the V_m, and the E_{rev} estimated from the linear fit of the data in an interval of ±20 mV around the point where the current reversed (5-7).

Current versus $[Ca^{2+}]_i$ relationship:

The $[Ca^{2+}]_i$–response relationships were fitted with the Hill–Langmuir equation of the form:

$$\frac{I}{I_{max}} = Base + \frac{1-Base}{1+\left(\frac{EC_{50}}{[Ca^{2+}]}\right)^{h}} \quad \text{[Suppl. Eq 1]}$$

where I is the current obtained at +70 mV in response to a given $[Ca^{2+}]_i$, I_{max} is the asymptotic current at saturating $[Ca^{2+}]_i$, EC_{50} is the $[Ca^{2+}]_i$ that causes half-maximal current activation, h is the slope factor (Hill coefficient) and *Base* is the pedestal of the curve.

Separation of the inhibitory and activating effects of A9C on the TMEM16A channel during concentration jump experiments:
To separate the inhibitory and activating effects of A9C on wild-type and mutant TMEM16A channels, whole-cell currents were measured at +70 mV in the absence or presence of $[Ca^{2+}]_i$ while A9C (300 μM) was rapidly applied to the cell ('concentration jump'), using an experimental design we developed in our previous study (7).

During fast application of A9C, in the presence of intracellular Ca^{2+}, the TMEM16A (wild-type, Q645A and I637A) whole-cell current amplitude rapidly declined to then increase to a new steady-state level. As A9C was washed-out, a dramatic increase in the current was observed followed by a return of the current to the level measured in the absence of A9C. These phenomena were interpreted as the combination of an inhibiting (block) and activating effect of A9C on TMEM16A channels. The initial decline in current at the start of the concentration jump is consistent with open-channel block by A9C, and the subsequent current potentiation is suggestive of a slower allosteric effect on channel gating caused by A9C (7). The rapid washout of A9C produced a fast relief of channel block, while the allosteric activating effect appeared to persist (7).

According to this idea, the initial current in the absence of A9C (I_0 in Fig. 3) is given by:

$$I_0 = NiP_o \quad \text{[Suppl. Eq 2]}$$

where N is the number of channels, i the single channel current and P_o is the channel open probability.

In the simplest scenario, the inhibition (block) can be described in terms of the probability of the channel of being blocked (p_b) while the enhancing effect can be accounted for by an activating factor (f_a). Thus, the inhibitory effect of A9C was estimated by back extrapolating the current amplitude (I_b) to the point when the drug was added, and it can be described as:

$$I_b = NiP_o p_b \quad \text{[Suppl. Eq 3]}$$

Assuming that immediately after washout the block is relieved but the potentiation initially persists, the initial current after washout is:

$$I_a = NiP_o f_a \quad \text{[Suppl. Eq 4]}$$

Thus, I_b/I_0 and I_a/I_0 offer an estimate of the p_b and f_a, respectively.

Assessment of Cl^- saturation and binding:
The apparent affinity of the Cl^- to the binding site(s) within the pore of the TMEM16A channel was determined with a stimulation protocol and solutions that favour unidirectional Cl^- flux through the pore of the channel. Whole-cell currents were recorded in response to 1 s V_m steps from +70 to +140 mV in 10 mV increments elicited every 2.5 s from a holding V_m of 0 mV and in the presence of various extracellular Cl^- concentrations ($[Cl^-]_o$).

The current *versus* $[Cl^-]_o$ relationship at various V_m was fitted with a Hill equation of the form:

$$I = Base + \frac{Max - Base}{1 + \left(\frac{K0.5}{[Cl]}\right)^l} \qquad \text{[Suppl. Eq 5]}$$

where *I* is the whole-cell current, *Base* is the pedestal of the curve, *Max* is the maximal asymptotic value of the curve, $K_{0.5}$ is the apparent dissociation constant for Cl^- and *l* is the slope factor (Hill coefficient). *I* was normalised for the maximal asymptotic value obtained in the presence of the highest V_m before display.

To investigate the functional interaction between intracellular Ca^{2+} and extracellular A9C, we calculated the $K_{0.5}$ for Cl^- binding within the pore under conditions in which intracellular Ca^{2+} and extracellular A9C were either absent or present (one at the time or simultaneously). Under our experimental conditions of unidirectional inward Cl^- fluxes, the inward Cl^- flux (J_{Cl}) (in mol/s) is related to $[Cl^-]_o$ following a rectangular hyperbola as:

$$J_{Cl} = J_{max} \frac{[Cl]_o}{[Cl]_o + K_{0.5}} \qquad \text{[Suppl. Eq 6]}$$

where J_{max} is the maximal flux during saturating $[Cl]_o$ at a given V_m. Multiplication of J_{Cl} for the Faraday constant enables expression of Suppl. Eq 6 in terms of Cl^- current (I_{Cl}) as:

$$I_{Cl} = I_{max} \frac{[Cl]_o}{[Cl]_o + K_{0.5}} \qquad \text{[Suppl. Eq 7]}$$

where I_{max} is the maximal current observed in the presence of saturating $[Cl^-]_o$ at a given V_m. $K_{0.5}$ is the $[Cl^-]_o$ at which I_{Cl} is half-maximal; thus, it provides an index of Cl^- transport within the pore.

To examine the cross-influence of Ca^{2+} and A9C on Cl^- binding within the pore we considered the following thermodynamic cycle.

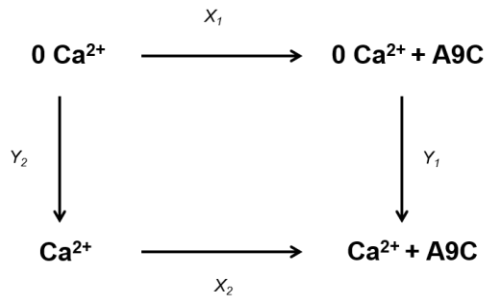

Each corner of the cycle refers to measurements of $K_{0.5}$ obtained in different conditions: (i) 0 $[Ca^{2+}]_i$ ('0 Ca^{2+}'); (ii) 0 $[Ca^{2+}]_i$ and 300 µM A9C ('0 Ca^{2+} + A9C'); (iii) 0.1 µM $[Ca^{2+}]_i$ ('Ca^{2+}') and (iv) 0.1 µM $[Ca^{2+}]_i$ and 300 µM A9C ('Ca^{2+} + A9C'). The letters X and Y on each arrow indicate the fold change in $K_{0.5}$ between the conditions linked by the arrow. For instance, X_1 is equal to $K_{0.5}(0\ Ca^{2+})/\ K_{0.5}(0\ Ca^{2+}\ +\ A9C)$.

The overall change in affinity between the '0 Ca^{2+}' condition (top left corner in the diagram of the cycle) and the 'Ca^{2+} + A9C' condition (bottom right corner) must be the same regardless of the pathway taken; that is:

$$X_1 \times Y_1 = X_2 \times Y_2 \qquad \text{[Suppl. Eq 8]}$$

Rearranging Suppl. Eq 8 leads to the definition of a coupling coefficient, Ω, as:

$$\Omega = \frac{X_1}{X_2} = \frac{Y_2}{Y_1} = \frac{K_{0.5}(0\ Ca^{2+}) \times K_{0.5}(100\ Ca^{2+}+A9C)}{K_{0.5}(100\ Ca^{2+}) \times K_{0.5}(0\ Ca^{2+}+A9C)} \qquad \text{[Suppl. Eq 9]}$$

If the two ligands have an independent effect on Cl^- fluxes, Ω will be equal to 1 (i.e. in the case A9C alters the $K_{0.5}$ for Cl^- binding by the same extent in the absence or presence of Ca^{2+} this would result in $X_1 = X_2$ and thus Ω = 1). If the Ca^{2+} and A9C interact to modulate Cl^- fluxes, then Ω will differ from 1. In energetic terms, the degree of functional interaction between Ca^{2+} and A9C ($\Delta\Delta G_{int}$) is given by:

$$\Delta\Delta G = -RTln(\Omega) \qquad \text{[Suppl. Eq 10]}$$

Molecular modelling

All molecular modelling was performed using a combination of Swiss-Model (8) and PyMOL (Schrodinger LLC, 2015). To generate a model of the open TMEM16A channel, we used a combination of the mammalian Ca^{2+}-bound TMEM16K (PDB ID: 5OC9) (9) and TMEM16A (PDB ID: 5OYB) (10) structures as templates. In the resulting model, the majority of the structure of TMEM16A was maintained, while the position of the TM4 helix was adjusted based on the TMEM16K structure. The conformation of this helix was carefully transplanted, without steric clashes from the TMEM16K-based structure (5OC9) to the original Ca^{2+}-bound state of TMEM16A (5OYB). To validate this open-state model of TMEM16A, we considered three criteria: (i) the structural similarity to the existing cryo-

EM structures/models using a static comparison of C_α root mean square deviation (r.m.s.d.); (ii) the stability of the local secondary and tertiary structure using C_α root mean square fluctuation (r.m.s.f.) analysis through 200 ns of MD simulation, and (iii) conduction of water molecules and Cl^- ions through the pore.

Coarse-grained MD preparation for atomistic simulation

The simulation systems were initially set-up using coarse-grained MD (CG-MD) simulations. All structures were converted to CG representation, and embedded in a palmitoyl oleoyl phosphatidylcholine (POPC) bilayer, solvated in water and 0.15 M NaCl using *insane* (11, 12). All simulations were carried out with the Martini2.3 biomolecular forcefield (13). The tertiary and quaternary structures of the protein were maintained through the application of an elastic network with a force constant of 1,000 kJ mol^{-1} nm^{-2} between CG backbone particles within 0.5-0.9 nm. Systems were energy minimised using the steepest descents algorithm and equilibrated for 500 ns. A temperature of 323 K was maintained throughout the simulation. For all simulations, the V-rescale temperature coupling was used (14), and a pressure of 1 atm was maintained using semi-isotropic Parrinello-Rahman pressure coupling (15). All simulations were carried out using GROMACS-2020.1 (16).

All-atom MD simulations and water accessibility inside the pore

The final time-point of the simulated CG systems were converted to all-atom using CG2AT (17), with the original protein structure aligned with the coordinates of the protein from the CG simulation (18). All simulations were carried out using the CHARMM36 biomolecular force-field (19). Virtual sites were applied to the CH_3 and NH_3^+ groups of the proteins and lipids (19, 20), allowing an integration time-step of 4 fs in the production runs. Simulations were energy minimised using the steepest descents algorithm, with simulations performed at a temperature of 310 K. In all simulations, distances were calculated using GROMACS-2020.1. The systems were equilibrated for 20 ns with position restraints imposed on the C_α backbone of the protein. Data were collected from 800 ns simulations (3 repeats) with and without Ca^{2+} present in its binding site. To calculate water accessibility into the pore, we used the last 100 ns of the simulation trajectory to calculate an occupancy of the water molecule (3 Å radii) using VolMap packages in VMD1.9.4 every 1 ns frame (21). All images were processed using PyMOLv2.1 (22).

Identification of Cl^- and A9C binding sites in the pore

In our 800 ns simulations with bound Ca^{2+}, we identified a central binding site for Cl^-. However, we could not observe full ion translocation from one side of the membrane to the other. This appears to be due to Cl^- preferentially binding to a central site during the simulations, in agreement to a previous study (23). The central Cl^- binding site was identified using VolMap tool in VMD based on the occupancy of the Cl^- in the pore over the simulation trajectory. To observe a full ion permeation path, Cl^- was placed on both the outer and the inner sides of the pore and simulated for 50 ns with 3 repeats to determine the paths towards the central binding site. The systems were energy minimised using the steepest descents followed by a 5 ns equilibration for the system, where the C_α backbone on the protein and the Cl^- was restrained with 1000 kJ mol^{-1} nm^{-2} with a 4 fs time-step. From these simulations we tracked the motions of the ions towards the central binding site.

To identify the A9C binding site, an A9C molecule was placed at the outer mouth of the pore using AutoDock Vina (24). The A9C was deprotonated, and the partial charges were assigned using Maestro (Schrödinger Release 2021-1: Maestro, Schrödinger, LLC, New York, NY, 2021). To place A9C at the outer mouth with no steric clashes, we centered the grid space on the extracellular half of the Ca^{2+}-bound open-state of the TMEM16A channel with a search space of 76x76x88 $Å^3$ for 20 iterations. This initial binding site for A9C, on the extracellular side, was used for the subsequent simulations to identify if A9C could permeate further into the pore. The simulation parameters for A9C were generated using CHARMM-GUI (25). The systems were energy minimised, before a 20 ns equilibration during which the C_α backbone on the protein and all atoms of the A9C molecules were restrained by 1000 $kJmol^{-1}nm^{-2}$. Data were collected from 200 ns simulations (3 repeats), which was an adequate duration for A9C to adopt a stable binding pose in the pore.

Statistics

Electrophysiological data were analysed with IgorPro (Wavemetrics, USA) software. Statistical significance was determined with two-tailed paired or unpaired t-tests or One-Way ANOVA with Bonferroni's post-test, as appropriate. For all statistical tests, P-values <0.05 were considered significant. Excel (Microsoft, USA) and SPSS (IBM, USA) were used for statistical analysis. Data are given as mean ± SEM alongside the number of independent experiments (n) with the exception of (i) the data in figure 3C, 4E, 7E and S10 which are presented with box plots (where the central mark indicates the median, the bottom and top edges of the box indicate the 25th and 75th percentile respectively, and the whiskers extend to the most extreme data points not considered outliers) and (ii) the values of Ω (Fig. 5C) which were calculated from average values of $K_{0.5}$ using Suppl. Eq 9. The uncertainties (δ) for Ω values were calculated using (26):

$$\frac{\delta_{f(a,b)}}{|f(a,b)|} = \sqrt{\left(\frac{\delta_a}{|a|}\right)^2 + \left(\frac{\delta_b}{|b|}\right)^2} \qquad \text{[Suppl. Eq 11]}$$

Where *a* and *b* refer to $K_{0.5}$ that were either multiplied or divided in Suppl. Eq 9.

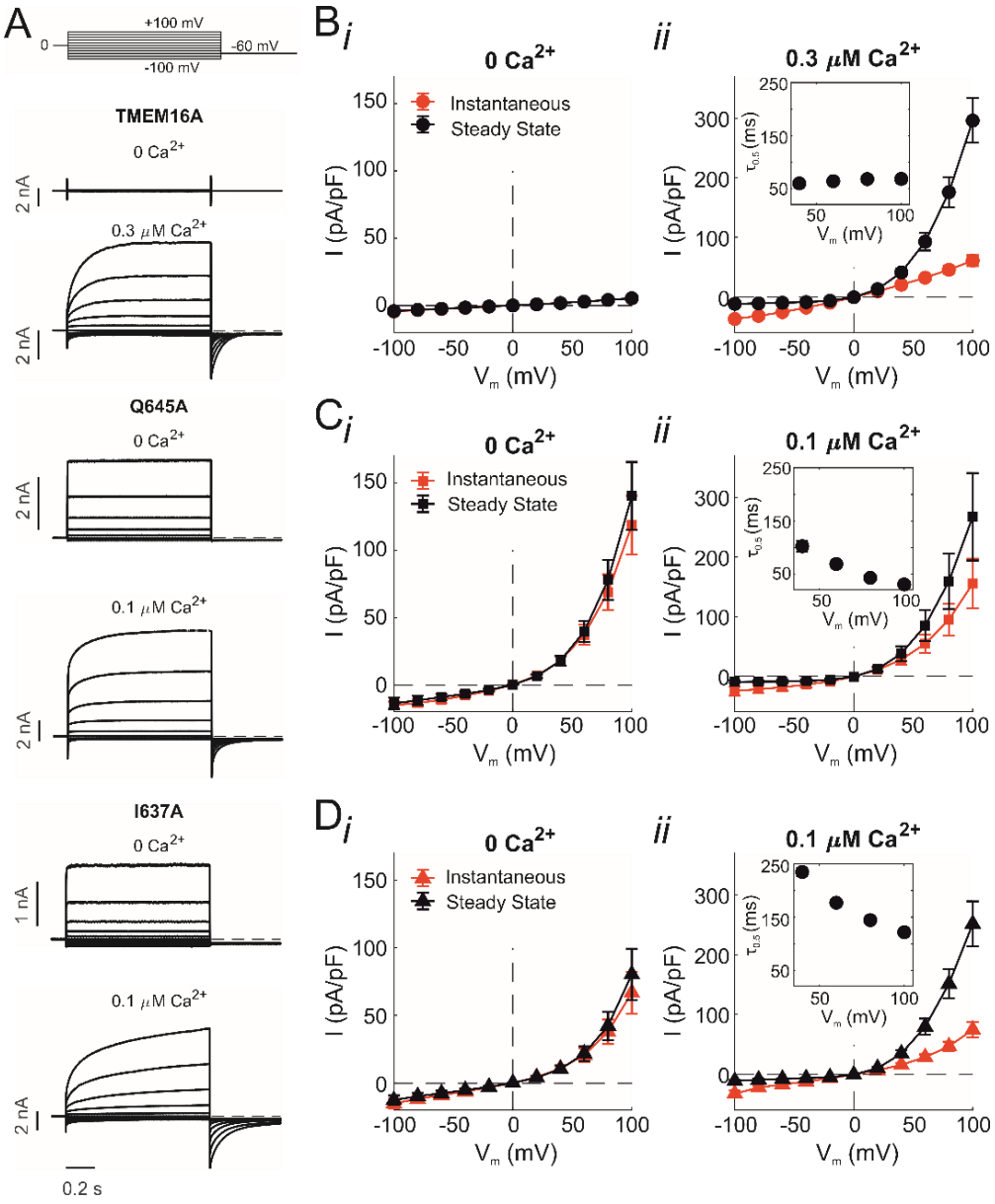

Fig. S1. IV relationships for TMEM16A, TMEM16A-Q645A and TMEM16A-I637A channels

(A)Whole-cell currents recorded from HEK-293T cells expressing TMEM16A, TMEM16A-Q645A or TMEM16A-I637A channels, in the absence or presence of Ca^{2+}, as indicated. Dashed horizontal lines represent zero-current level. The stimulation protocol is shown in the top left-hand corner. (B) Mean whole-cell TMEM16A current density *versus* V_m relationships measured at the beginning (Instantaneous, in red) or end (Steady state, in black) of 1 s V_m pulses from -100 to +100 mV in 20 mV increments in the (i) absence (n=9) or (ii) presence (n=11) of intracellular Ca^{2+}, as indicated. (C) Mean instantaneous and steady state whole-cell TMEM16A-Q645A current density *versus* V_m relationships obtained (i) in the absence (n=21) or (ii) presence (n=14) of intracellular Ca^{2+}, as indicated. (D) Mean instantaneous and steady state whole-cell TMEM16A-I637A current density

versus V_m relationships obtained in the (i) absence (n=17) or (ii) presence (n=16) of intracellular Ca^{2+}, as indicated. Insets in (Bii), (Cii) and (Dii) show mean $\tau_{0.5}$ of current activation (filled symbols) at various V_m.

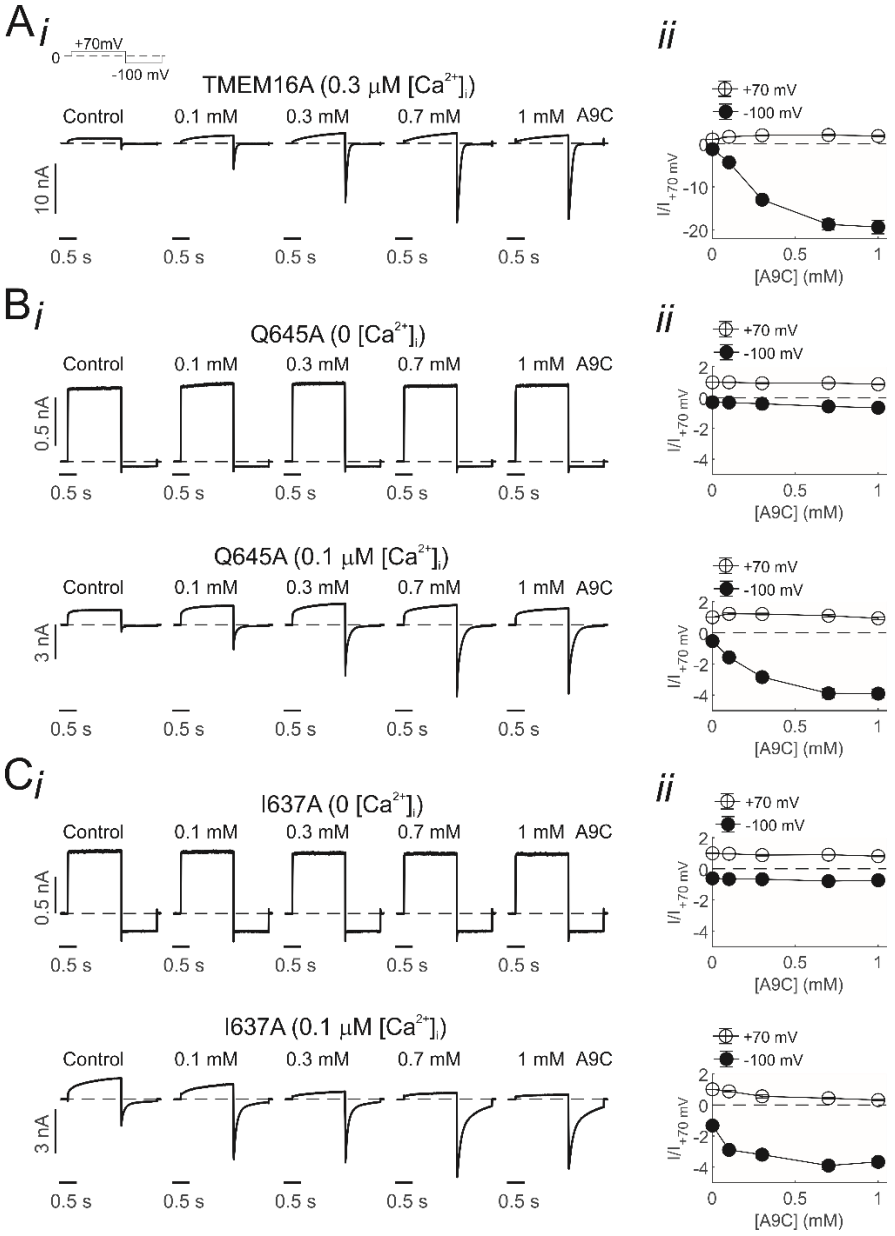

Fig. S2. Effects of extracellular A9C on whole-cell TMEM16A, TMEM16A-Q645A and TMEM16A-I637A currents

Panels (A-C) (i) Whole-cell currents recorded from HEK-293T cells expressing TMEM16A (A), TMEM16A-Q645A (B), TMEM16A-I637A (C) in the absence (control) or presence of various extracellular [A9C], and the indicated $[Ca^{2+}]_i$. Dashed horizontal lines indicate the zero-current level. The stimulation protocol is shown in the top left-hand corner in A. (ii) Mean steady-state current measured at +70 mV (open symbols) or mean peak current measured at -100 mV (filled symbols), normalised for the steady-state current measured at +70 mV in the absence of A9C, and plotted *versus* [A9C]. The number of experiments was 6-8 in each case.

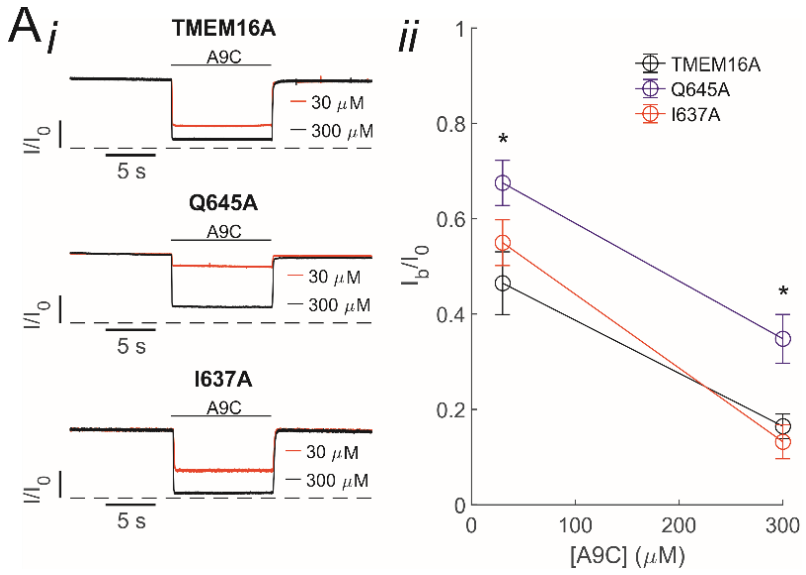

Fig. S3. Effects of extracellular A9C on TMEM16A, TMEM16A-Q645A and TMEM16A-I637A currents in the presence of high $[Ca^{2+}]_i$

(A) (i) Whole-cell currents recorded from HEK-293T cells expressing TMEM16A, TMEM16A-Q645A or TMEM16A-I637A channels, as indicated. V_m was +70 mV and $[Ca^{2+}]_i$ was 12.5 µM. Extracellular A9C (30 µM or 300 µM, as indicated) was applied via a fast-perfusion system ('concentration jump') as indicated by the horizontal bars. Dashed horizontal lines indicate the zero-current level. (ii) Mean relationship between [A9C] and current amplitude, expressed relative to the current measured in the absence of the drug (I_b/I_0) for each channel type, as indicated. The number of experiments was 5-11 in each case. *P<0.05, compared to TMEM16A.

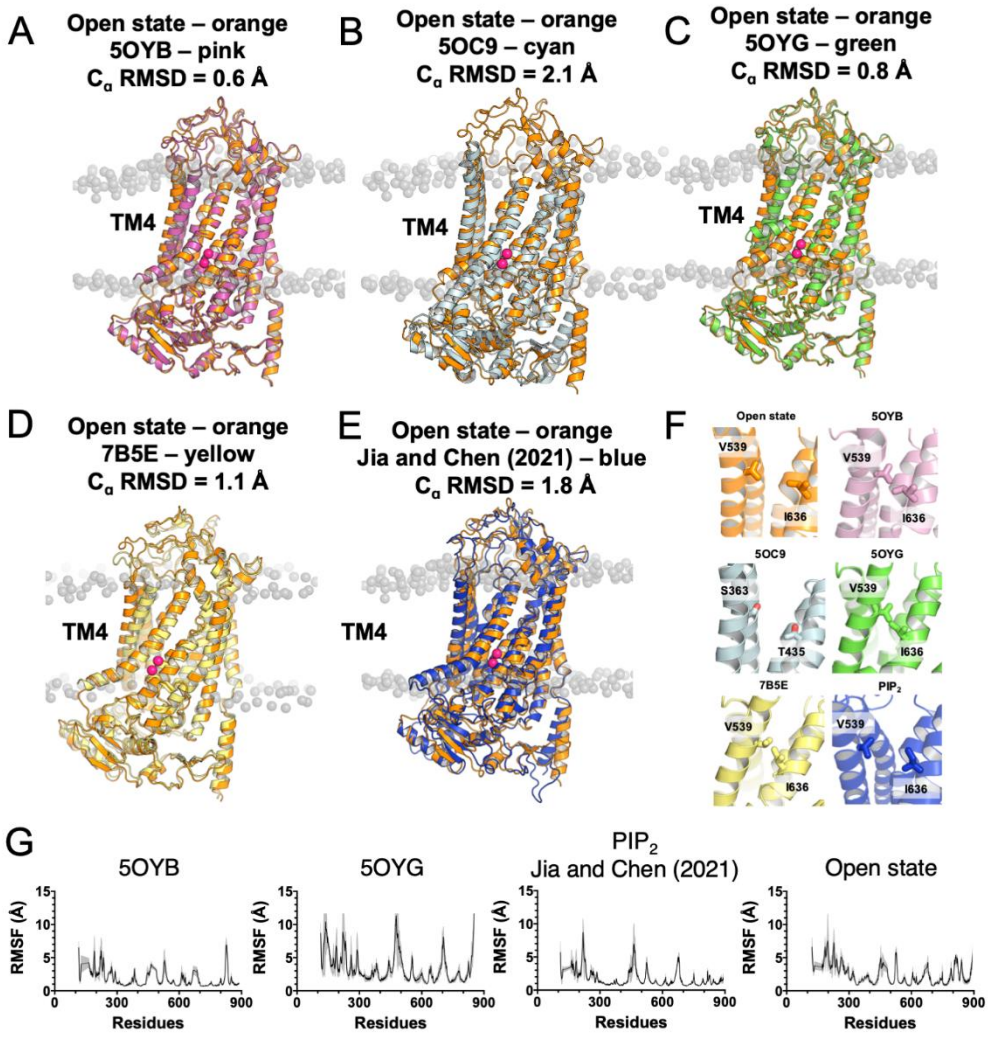

Fig. S4. Structural alignment between the open-state model and the existing structures

The open-state model (orange) is aligned with (A) Ca^{2+}-bound TMEM16A cryo-EM structure (5OYB, pink), (B) Ca^{2+}-bound TMEM16K structure (5OC9, cyan), (C) Ca^{2+} free TMEM16A cryo-EM structure (5OYG, green), (D) 7B5E Ca^{2+}-bound TMEM16A I551A mutant cryo-EM structure (yellow) and (E) the model of PIP_2-bound open TMEM16A channel by Jia & Chen (2021) (blue). (F) Zoom in of the channels' outer gate to illustrate the relative position of V539 and I636 in the different cryo-EM structures and models, as indicated. (G) C_α r.m.s.f. of the cryo-EM structures and the existing models sampled every 10 ps. The shaded region indicates the standard deviation around the mean of three repeats.

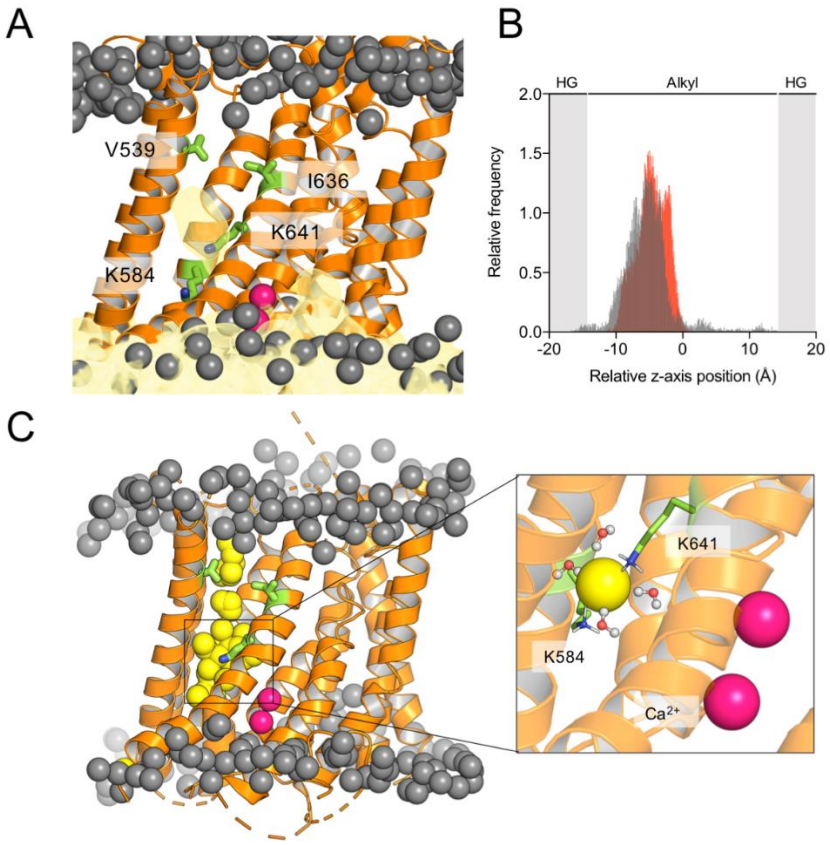

Fig. S5. Cl^- binding site in the TMEM16A channel

(A) Calculations of the average density of Cl^- inside the pore of the model of the open TMEM16A channel over the 800 ns trajectory using VolMap. The occupancy of Cl^- is shown in yellow. The phosphate headgroups are shown in dark grey sphere, the protein is represented as cartoon in orange, relative position of V539, I636, K584 and K641 are shown in green and Ca^{2+} are shown in pink. (B) Histogram of the relative position of Cl^- within the model of the open TMEM16A channel across 50 ns simulations (n=3) with the bin size of 0.08 Å and sampled every 10 ps. The starting position of the Cl^- was either on the extracellular (grey) or intracellular (red) side of the membrane. In either case, Cl^- reached the same central binding site during the course of the simulation. The regions shaded in gray denoted the positions of the phosphate headgroups. (C) Left panel: Overlay of snapshots of different Cl^- positions as it permeates through the pore. Right panel: Representative position of a Cl^- (yellow) at the end of a 50 ns of simulation. The residues that make contacts with Cl^- are shown in green, and the Ca^{2+} within the TMEM16A binding sites are shown in pink.

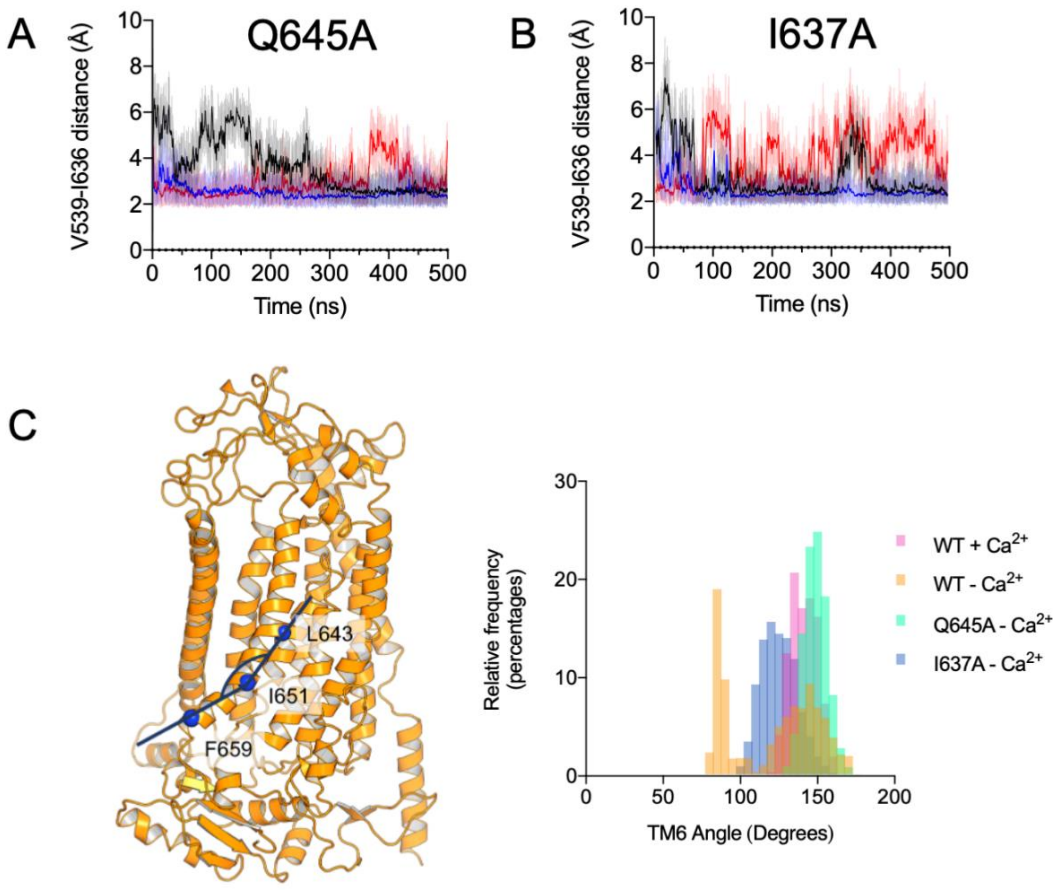

Fig. S6. Simulations of TMEM16A-Q645A and TMEM16A-I637A mutants

(A-B) The minimum distance between V539 and I636 in Q645A (A) and I637A (B) mutants simulations in the absence of Ca^{2+}. The lighter shaded line shows the distance calculated every 10 ps, and the darker line shows running averages over 1 ns. The different colors indicate the three independent repeats. (C) Left panel: Representative structure of the open-state model, showing the locations of L643, I651 and F659 on TM6. Right panel: Histogram of the angle distributions between the Cα atoms of L643-I651-F659 on TM6, representing the kinking of the TM helix over 500 ns of simulations of wild-type (orange), Q645A (green), and I637A (blue) channels in absence of Ca^{2+}. The comparison for the wild-type model in presence of Ca^{2+} is shown in purple. Histograms were sampled with the bin size of 5 degrees and sampled every 1 ns (n=3).

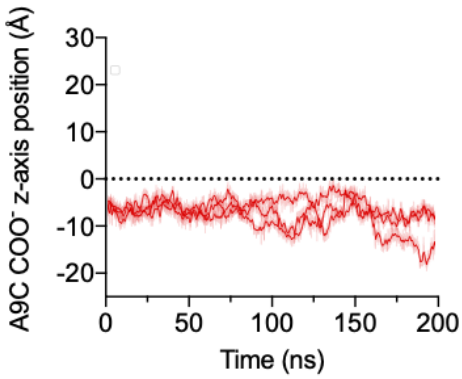

Fig. S7. Inability of intracellular A9C to reach a binding site within the pore of the open TMEM16A model

Z-axis position of A9C within the pore of the open TMEM16A model generated in this study. The simulations were run in presence of intracellular Ca^{2+}. A9C was applied to the intracellular side. In three repeats of 200 ns simulation the A9C did not translocate to and reached the putative binding site.

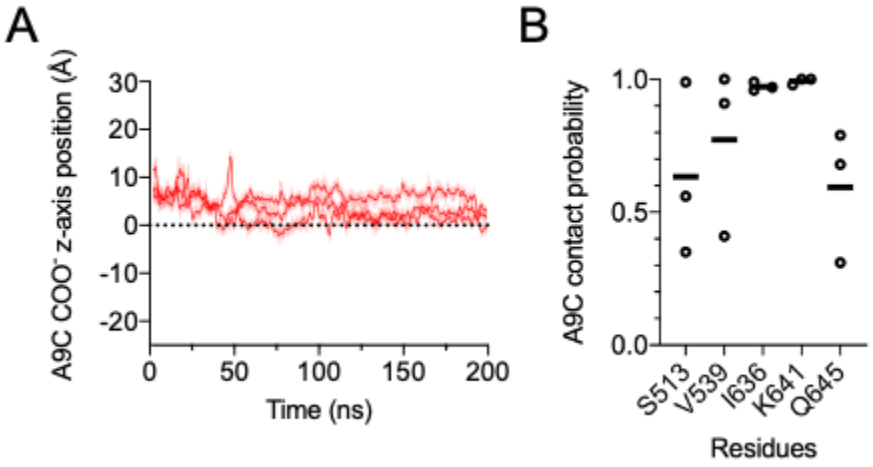

Fig. S8. Entry of extracellular A9C into the pore of the PIP_2-bound TMEM16A model

(A) z-axis position of A9C within the pore of PIP_2-bound model of the open TMEM16A channel described in (27). The simulations were run in presence of intracellular Ca^{2+}. A9C was applied extracellularly. (B) Contact probability across 3 repeats in the last 100 ns of the 200 ns simulation trajectory with the same residues identified in Fig. 7A.

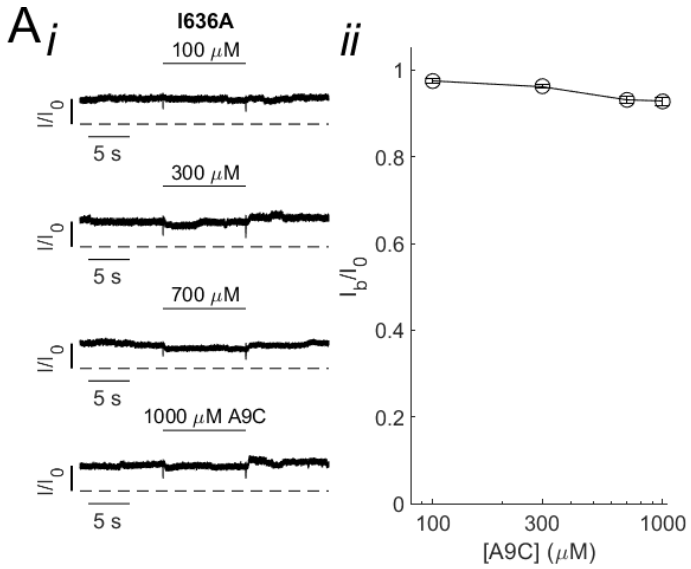

Fig. S9. Whole-cell TMEM16A-I636A currents are unaffected by extracellular A9C

(A) (i) Representative whole-cell currents recorded from a HEK-293T cell expressing TMEM16A-I636A channels. V_m was +70 mV and $[Ca^{2+}]_i$ was 0.3 µM $[Ca^{2+}]_i$. Extracellular A9C was applied via a fast-perfusion system ('concentration jump') as indicated by the horizontal bars. Dashed horizontal lines indicated the zero-current level. (ii) Mean relationship between extracellular [A9C] and the current amplitude expressed relative to the current measured in the absence of the drug (I_b/I_0). The number of experiments was 5 in each case.

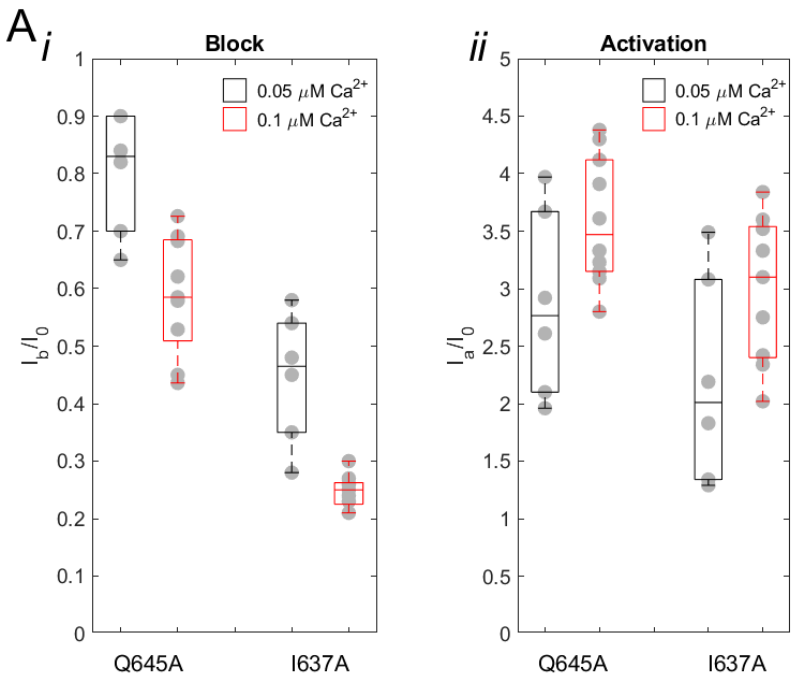

Fig. S10. Inhibiting and activating effects of A9C in the presence of various $[Ca^{2+}]_i$.
(A) Mean current inhibition (I_b/I_0, (i)) and activation (I_a/I_0, (ii)) plotted for each channel type in box plots, as indicated. $[Ca^{2+}]_i$ was 0.05 µM (black) or 0.1 µM (red). The data obtained in 0.1 µM $[Ca^{2+}]_i$ are replotted form Fig. 3C. The number of experiments was 5-9 in each case.

Table S1: Parameters (EC_{50}, h and Base) obtained from the Hill fit (Suppl. Eq. 1) of the $[Ca^{2+}]_i$-response relationships for currents mediated by TMEM16A, TMEM16A-Q645A, TMEM16A-I637A, TMEM16A-Q645A-E650A and TMEM16A-Q645A-E650R channels.

	EC_{50} (µM)	h	Base
TMEM16A	0.72 ± 0.04 (n=10)	3.00 ± 0.24 (n=10)	0.004 ± 0.004 (n=10)
Q645A	0.22 ± 0.02* (n=9)	2.61 ± 0.42 (n=9)	0.16 ± 0.04* (n=9)
I637A	0.19 ± 0.02* (n=7)	2.13 ± 0.37 (n=7)	0.28 ± 0.06* (n=7)
Q645AE650A	0.63 ± 0.11 (n=9)	0.93 ± 0.07* (n=9)	0.27 ± 0.05* (n=9)
Q645AE650R	0.93 ± 0.14 (n=9)	0.96 ± 0.07* (n=9)	0.19 ± 0.03* (n=9)

* indicates statistically significant difference from TMEM16A. (P< 0.05).

Table S2: Ratio between steady state and instantaneous current (I_{ss}/I_{nst}) and rectification index (I_{100}/I_{-100}) for TMEM16A, TMEM16A-Q645A and TMEM16A-I637A currents measured in the absence or presence of $[Ca^{2+}]_i$.

	I_{ss}/I_{inst}	I_{100}/I_{-100}
TMEM16A	5.1 ± 0.3 (n=11)	-28.8 ± 3.1 (n=11)
TMEM16A-Q645A 0 $[Ca^{2+}]_i$	1.2 ± 0.0* (n=21)	-16.1 ± 2.4* (n=21)
TMEM16A-Q645A 0.1 µM $[Ca^{2+}]_i$	1.9 ± 0.1* (n=14)	-27.5 ± 2.8 (n=14)
TMEM16A-I637A 0 $[Ca^{2+}]_i$	1.2 ± 0.0* (n=17)	-7.5 ± 0.9* (n=17)
TMEM16A-I637A 0.1 µM $[Ca^{2+}]_i$	3.6 ± 0.2* (n=16)	-27.2 ± 3.1 (n=16)

* indicates statistically significant difference from TMEM16A. (P < 0.05).

Movie S1.

MD simulation (800 ns) of the TMEM16A open-state model with bound Ca^{2+}. V539 and I636 residues that form the constriction point at the outer pore of the channel in the closed-state of the channel are shown as green sticks. Ca^{2+} ions are shown as pink spheres. The phosphorus atoms of the phospholipid membrane are shown as grey, semi-transparent spheres. In this state the channels remain conductive to solvent.

Movie S2.

MD simulation (800 ns) of the TMEM16A open-state model without bound Ca^{2+}. V539 and I636 residues that form the constriction point at the outer pore in the closed-state of the channel are shown as green sticks. Ca^{2+} ions are shown as pink spheres. The phosphorus atoms of the phospholipid membrane are shown as grey, semi-transparent spheres. Without Ca^{2+} the channel is close at the outer pore, with V539 and I636 residues moving closer together to constrict the pore.

SI References

1. A. Caputo *et al.*, TMEM16A, A Membrane Protein Associated with Calcium-Dependent Chloride Channel Activity. *Science* **322**, 590-594 (2008).
2. K. J. Smith *et al.*, Coronary spasm and acute myocardial infarction due to a mutation (V734I) in the nucleotide binding domain 1 of ABCC9. *Int J Cardiol* **168**, 3506-3513 (2013).
3. M. E. Jurman, L. M. Boland, Y. Liu, G. Yellen, Visual identification of individual transfected cells for electrophysiology using antibody-coated beads. *Biotechniques* **17**, 876-881 (1994).
4. B. Manoury, A. Tamuleviciute, P. Tammaro, TMEM16A/Anoctamin 1 protein mediates calcium-activated chloride currents in pulmonary arterial smooth muscle cells. *The Journal of Physiology* **588**, 2305-2314 (2010).
5. A. Adomaviciene, K. J. Smith, H. Garnett, P. Tammaro, Putative pore-loops of TMEM16/anoctamin channels affect channel density in cell membranes. *The Journal of Physiology* **591**, 3487-3505 (2013).
6. P. Tammaro, S. V. Smirnov, O. Moran, Effects of intracellular magnesium on Kv1.5 and Kv2.1 potassium channels. **34**, 42-51 (2005).
7. C. M. Ta, A. Adomaviciene, N. J. Rorsman, H. Garnett, P. Tammaro, Mechanism of allosteric activation of TMEM16A/ANO1 channels by a commonly used chloride channel blocker. *British journal of pharmacology* **173**, 511-528 (2016).
8. A. Waterhouse *et al.*, SWISS-MODEL: homology modelling of protein structures and complexes. *Nucleic Acids Res* **46**, W296-W303 (2018).
9. S. R. Bushell *et al.*, The structural basis of lipid scrambling and inactivation in the endoplasmic reticulum scramblase TMEM16K. *Nature Communications* **10**, 3956 (2019).
10. C. Paulino, V. Kalienkova, A. K. M. Lam, Y. Neldner, R. Dutzler, Activation mechanism of the calcium-activated chloride channel TMEM16A revealed by cryo-EM. *Nature* **552**, 421-425 (2017).
11. L. Monticelli *et al.*, The MARTINI Coarse-Grained Force Field: Extension to Proteins. *Journal of Chemical Theory and Computation* **4**, 819-834 (2008).
12. T. A. Wassenaar, H. I. Ingólfsson, R. A. Böckmann, D. P. Tieleman, S. J. Marrink, Computational Lipidomics with insane: A Versatile Tool for Generating Custom Membranes for Molecular Simulations. *Journal of Chemical Theory and Computation* **11**, 2144-2155 (2015).
13. S. J. Marrink, H. J. Risselada, S. Yefimov, D. P. Tieleman, A. H. de Vries, The MARTINI force field: coarse grained model for biomolecular simulations. *J Phys Chem B* **111**, 7812-7824 (2007).
14. G. Bussi, D. Donadio, M. Parrinello, Canonical sampling through velocity rescaling. *The Journal of Chemical Physics* **126**, 014101 (2007).
15. M. Parrinello, A. Rahman, Polymorphic transitions in single crystals: A new molecular dynamics method. *Journal of Applied Physics* **52**, 7182-7190 (1981).
16. M. J. Abraham *et al.*, GROMACS: High performance molecular simulations through multi-level parallelism from laptops to supercomputers. *SoftwareX* **1-2**, 19-25 (2015).

17. O. N. Vickery, P. J. Stansfeld, CG2AT2: An Enhanced Fragment-based approach for Serial Multi-scale Molecular Dynamics simulations. *bioRxiv* 10.1101/2021.03.25.437005, 2021.2003.2025.437005 (2021).
18. P. J. Stansfeld, M. S. P. Sansom, From Coarse Grained to Atomistic: A Serial Multiscale Approach to Membrane Protein Simulations. *Journal of Chemical Theory and Computation* **7**, 1157-1166 (2011).
19. J. Huang, A. D. Mackerell, CHARMM36 all-atom additive protein force field: Validation based on comparison to NMR data. *Journal of Computational Chemistry* **34**, 2135-2145 (2013).
20. B. Loubet, W. Kopec, H. Khandelia, Accelerating All-Atom MD Simulations of Lipids Using a Modified Virtual-Sites Technique. *Journal of Chemical Theory and Computation* **10**, 5690-5695 (2014).
21. W. Humphrey, A. Dalke, K. Schulten, VMD: Visual molecular dynamics. *Journal of Molecular Graphics* **14**, 33-38 (1996).
22. Schrodinger, LLC (2015) The PyMOL Molecular Graphics System, Version 1.8.
23. Z. Jia, J. Chen, Specific PIP_2 binding promotes calcium activation of TMEM16A chloride channels. *Communications Biology* **4**, 259 (2021).
24. O. Trott, A. J. Olson, AutoDock Vina: Improving the speed and accuracy of docking with a new scoring function, efficient optimization, and multithreading. *Journal of Computational Chemistry* 10.1002/jcc.21334, NA-NA (2009).
25. S. Kim *et al.*, CHARMM-GUI ligand reader and modeler for CHARMM force field generation of small molecules. *Journal of Computational Chemistry* **38**, 1879-1886 (2017).
26. H. H. Ku, Notes on Use of Propagation of Error Formulas. *J Res Nbs C Eng Inst* **C 70**, 263-273 (1966).
27. Z. Jia, J. Chen, Specific PIP_2 binding promotes calcium activation of TMEM16A chloride channels. *Commun Biol* **4**, 259 (2021).